the Anti–Lung Cancer Association (ALCA), a for-profit organization for lung cancer screening.[20,21] Each screening consisted of a low-dose helical CT examination, chest radiography, and cytologic sputum studies. During this period, a total of 15,938 low-dose helical CT examinations were performed in 2052 ALCA members. Among the low-dose helical CT examinations, a total of 1566 CT examinations were judged as having abnormal findings requiring further examination. Sixty-seven cases of lung cancer (peripheral-type lung cancer, 61; hilar-type lung cancer, 6) were detected during the ALCA lung cancer screening project. Out of these 67 cases, 51 cases (76%) were pathologic stage IA. The treatments used in the 67 cases were as follows: surgery (n = 55), radiotherapy (n = 5), radiotherapy and chemotherapy (n = 2), chemotherapy (n = 4), and photodynamic therapy (n = 1). Among the patients with peripheral nodules detected by the low-dose helical CT examinations performed every 6 months, the patients with histologically diagnosed nodules exhibiting pGGO larger than 5 mm in diameter at the time of the first thin-section CT and followed-up by thin-section CT for more than 6 months were enrolled in the current study.

CT Scanning Conditions

A TCT900S Superhelix CT scanner (Toshiba Medical Inc., Tokyo, Japan) was used for all of the examinations. Low-dose helical CT screening was performed under the following conditions: 120 kV, 50 mA, beam width of 10 mm, 1 rotation of the x-ray tube per second, and a table speed of 20 mm per second (pitch 2:1). Reconstruction was performed at intervals of 10 mm. The CT images were displayed on a monitor with a window width of 2000 HU and a window level of −700 HU. If newly developed nodules were identified, thin-section CT examinations were performed under the following conditions: 120 kV, 250 mA, beam width of 2 mm, 1 rotation of the x-ray tube per second, and a table speed of 2 mm per second (pitch 1:1). Reconstruction was performed at intervals of 2 mm using a thin-section CT algorithm.

Evaluation of pGGO Progression Patterns

The progression patterns were classified based on changes in the size and density of the pGGOs on the thin-section CT images. The study period was divided into 2 phases: the unidentified phase (ie, the period prior to the first thin-section CT scan) and the follow-up phase (ie, the period after the first thin-section CT scan). CT images of the pGGOs in the unidentified phase were reviewed independently by 4 physicians (R.K., M.K., H.O., K.E.), who are diagnostic experts in chest radiology, and by 1 radiologist (M.K.). CT findings were adopted as positive findings if 3 of more of the doctors agreed. After the independent reviews, we decided by consensus as to how many pGGOs were newly developed or had arisen from inconspicuous nodules during the helical CT screening period. In the follow-up phase, the size of the pGGOs was measured with a pair of calipers on the thin-section CT images obtained during the initial scan and the final scan by consensus of 2 diagnostic experts (R.K., M.K.) to assess doubling time. The size of the lesion was evaluated using measurements that passed through the center of the lesion. Size was defined as the average of the length and width of the lesion. Doubling times were calculated using the Schwartz equation.[22] The density of faint opacities was evaluated visually on the thin-section CT images obtained during the follow-up phase. pGGO was defined as a homogeneous GGO, and mixed GGO was defined as a GGO with a solid component.

Pathologic Classification of Adenocarcinomas

The histologic findings of the adenocarcinomas were classified according to the criteria of the World Health Organization (WHO)[23] and the criteria of Noguchi et al.[24] The classification system for replacement growth patterns developed by Noguchi et al is as follows: type A (localized bronchioloalveolar carcinoma; LBAC), type B (LBAC with foci of collapsed alveolar structure), and type C (LBAC with foci of active fibroblastic proliferation).

RESULTS

Patient Characteristics

Eight patients with pGGOs (6 men and 2 women) were enrolled in the current study (Table 1). The patients ranged in age from 49 to 69 years (mean, 64 years). With regard to smoking history, 3 patients were nonsmokers, 4 were ex-smokers, and 1 was a current smoker. Four of these 8 pGGO patients were not apparent during the initial screening and became apparent during the screening period, and 3 of the other 4 pGGO patients with inconspicuous opacities visible in retrospect during the initial screening became apparent later. In 1 other case, a conspicuous opacity and multiple old tuberculosis lesions were observed during the initial CT screening. The locations of the pGGOs were as follows: right upper lobe (n = 4), right lower lobe (n = 1), left upper lobe (n = 1), and left lower lobe (n = 2).

Clinical Course

The period between the first visible nodule of a pGGO on a thin-section CT image and the first visible opacity on a helical CT screening image when viewed retrospectively ranged from 13 to 46 months (mean, 22 months) (Table 1). The period between the first thin-section CT examination and the surgery ranged from 7 to 39 months (mean, 19 months). The interval between the last thin-section CT examination and surgery ranged from 1 to 98 days (mean, 32 days).

Histology of GGOs

Seven patients had bronchioloalveolar carcinoma (BAC), defined as noninvasive by the WHO classification in 1999, and 1 had an adenocarcinoma with mixed subtypes (Table 1). Based on Noguchi's classification for small adeno-

TABLE 1. Clinical Characteristics and Histology of Ground-Glass Opacities

Case No.	Sex	Age at Detection (Years)	Smoking Index	Development	Lobe	Period Between: First Visible and the First TS-CT (Months)*	Period Between: The First TS-CT and Surgery (Months)*	Period Between: The Last TS-CT and Surgery (Days)	Histology: WHO Classification	Histology: Noguchi Type
1	M	69	1300	New	RU	41	13	1	Ad	C
2	M	69	800 (ex)	New	RU	13	39	36	BAC	B
3	F	66	Non	New	LL	13	14	33	BAC	A
4	M	66	450 (ex)	New	LU	18	26	98	BAC	A
5	F	65	Non	ic	LL	46	28	13	BAC	B
6	M	69	800 (ex)	ic	RU	21	12	13	BAC	A
7	M	49	515 (ex)	ic	RU	14	10	6	BAC	A
8	M	63	Non	c	RL	13	7	57	BAC	B

Non, nonsmoker; ex, ex-smoker; ic, inconspicuous; c, conspicuous; RU, right upper lobe; LU, left upper lobe; LL, left lower-lobe; TS-CT, thin-section CT; BAC, bronchioloalveolar carcinoma; Ad, adenocarcinoma.
*Number of months was rounded.

carcinomas, the pGGOs consisted of 4 cases of type A and 2 cases of type B while the mixed GGOs consisted of 1 case of type B and 1 case of type C (Tables 1, 2). All the lung cancers were diagnosed at pathologic stage IA.

Progression of pGGOs

The period between the first thin-section CT and the final thin-section CT examinations ranged from 6 to 37 months (mean, 17 months) (Table 2). The opacities ranged in size from 6.5 mm to 17 mm (mean, 10 mm) at the time of the first thin-section CT examination and from 7 mm to 16.5 mm (mean, 10.5 mm) at the time of the final thin-section CT examination. The progressions of 8 opacities in the follow-up phase were classified into 3 types: increasing in size (Increasing type, n = 5), decreasing in size and the appearance of a solid component (decreasing type, n = 2), and stable in size and increasing in density (density type, n = 1). In addition, the decreasing type was classified into 2 subtypes: a rapid-decreasing type (case 1, Fig. 1; decrease in size at the time of the 6-month follow-up) and a slow-decreasing type (case 2, Fig. 2; decrease after follow-up for more than 1 year). All but 1 of the follow-up cases were noninvasive, and the remaining GGO with a solid component was judged to be minimally invasive adenocarcinoma because the size of the collapse fibrosis was only 2 mm in diameter (Fig. 1F).

TABLE 2. Thin-Section CT Findings, Progression Types, and Doubling Time of Ground-Glass Opacities

Case No.	Follow-Up Phase with Thin-Section CT: GGO Size (mm) First	GGO Size (mm) Final	Final TS-CT of GGO: Density	Solid	Finding	Progression Type	Period of Follow-Up with TS-CT (Months)*	GGO Doubling Time (Days)
1	17	12	Increasing	+	Mixed	Dec	12	−214
2	14	12	Increasing	+	Mixed	Dec	37	−1680
3	6.5	7.5	Stable	−	Pure	Inc	13	617
4	7	10.5	Stable	−	Pure	Inc	22	383
5	7	7	Increasing	−	Pure	Den	27	—
6	8.5	9.5	Stable	−	Pure	Inc	12	669
7	6.5	9	Stable	−	Pure	Inc	10	216
8	13.5	16.5	Stable	−	Pure	Inc	6	198

CT, computed tomography; GGO, ground-glass opacity; TS-CT, thin-section computed tomography; Inc, increasing; Dec, decreasing; Den, density.
*Number of months was rounded.

TABLE 3. Evolution of Solid Components in Ground-Glass Opacities

Case No.	Follow-Up Phase with TS-CT Solid Size (mm) First TS-CT	Months After the First TS-CT 6	11	23	36	Doubling Time (Days)
1	0*	8				14*
2	0	—	2	3	7.5	130†

TS-CT, thin-section computed tomography.
*Doubling time of solid component in case 1 was calculated on the assumption that the first size was 0.5 mm.
†Doubling time of solid component in case 2 was calculated based on the sizes between 11 months and 36 months after the first TS-CT.

Doubling Time

The doubling times of the increasing-type opacities ranged from 198 to 669 days (mean ± SD, 417 ± 220 days). The doubling time of the density-type opacity could not be calculated because it did not change in size. For the decreasing-type opacities, the doubling times were calculated based on the sizes of the pGGOs and the solid components, individually. In case 1, the doubling times of the pGGO and the solid component were −214 and 14 days, respectively. In case 2, the doubling times of the pGGO and the solid component were 1680 and 130 days, respectively.

Correlation of Thin-Section CT Images and Pathologic Findings

The pGGO corresponded to the lepidic growth of cancer cells (Fig. 1E), the thickening of the alveolar wall (Fig. 1E), and the collapse of the alveolar space (Fig. 1E). Solid components corresponded not only to the collapse of the alveolar space and fibrosis (Fig. 1F and Fig. 2G), but also to a severe narrowing of the alveolar space (Fig. 1F). With the development of a solid component in case 2, the distance between the surrounding pulmonary veins and the bronchus gradually narrowed (Figs. 2C–F). The same finding was observed in case 1 (Figs. 1C, D).

DISCUSSION

To our knowledge, this study is the first report to describe the progression of pGGOs in minute lung cancers that appeared as new pGGOs during the screening process or arose from inconspicuous minute nodules on low-dose helical CT screening images obtained at 6-month intervals. In addition, the progressions of the pGGOs on the thin-section CT images were classified into 3 types for the first time. Although a few papers have described the natural history of GGOs in pulmonary adenocarcinoma,[4,7,12,15–17] only 1 researcher[15] reported 2 GGOs that decreased in size, but the size reduction occurred in mixed GGOs, not in pGGOs. The rapid decreasing of a pGGO and the appearance of a solid component has not previously been reported.

Radiologic-pathologic correlations revealed that pGGOs on thin-section CT images mainly represent the lepidic growth of adenocarcinomas.[1,3,4,12,15–17] Solid components in the mixed GGOs were caused by the collapse of alveolar spaces or regions of fibrosis[12] and by a severe narrowing of the alveolar space (case 1). The narrowing of the distance between the surrounding pulmonary vessels and the bronchus was caused not only by the collapse of the alveolar space (cases 1 and 2), but also by the development of fibrosis (case 1) in the pGGO lesions. This finding has been termed "vessel convergence."[12,15,17] Based on our observations of the progression from a pure GGO to a mixed GGO in cases 1 and 2, our results also support the stepwise progression of replacement-type adenocarcinoma.[12,15,17]

Although 1 researcher raised serious questions about the concept of 2-year stability implying benignity,[25] pulmonary nodules are generally considered to be benign if they remain the same size or decrease in size over a 2-year observation period.[26,27] However, our results show that stability or reduction in size over a 2-year period does not necessarily indicate benignity. In the case of a pGGO that decreases in size, can the Schwartz equation be applied to a change from a pGGO to a mixed GGO if the area of the GGO decreases? Usually, the Schwartz equation is based on the assumption that constant exponential tumor growth is the basic pattern of neoplastic proliferation.[22] The doubling time for mixed GGOs has been reported to be 457 ± 260 days.[28] However, progression to a mixed GGO in a case where the pGGO decreases in size and a solid component simultaneously appears has not previously been reported. Moreover, the calculation of doubling times for each component in a mixed GGO has never, to the best of our knowledge, been performed prior to the current study. The doubling time for the solid component in case 1 was calculated based on the assumption that the initial size of the solid component was 0.5 mm, this because the thin-section CT images were taken not only by the single-slice CT scanner described above, but by a multislice CT scanner with the imaging parameters set at 0.5 mm × 4 rows and image reconstruction performed at 1-mm intervals.

Whether pGGOs should be resected or followed up is controversial. Definite evidence of the natural history of pGGOs does not exist at present. However, based on the indirect corroboration described below, we suggest that close follow-up until the appearance of a solid component may be a valid option for the management of pGGO. First, most pGGOs are either atypical adenomatous hyperplasia (preinvasive lesions according to the 1999 WHO criteria), BAC (a noninvasive lesion), or minimally invasive adenocarcinoma.[1,8,29] Second, 1 researcher[7] has previously reported information concerning

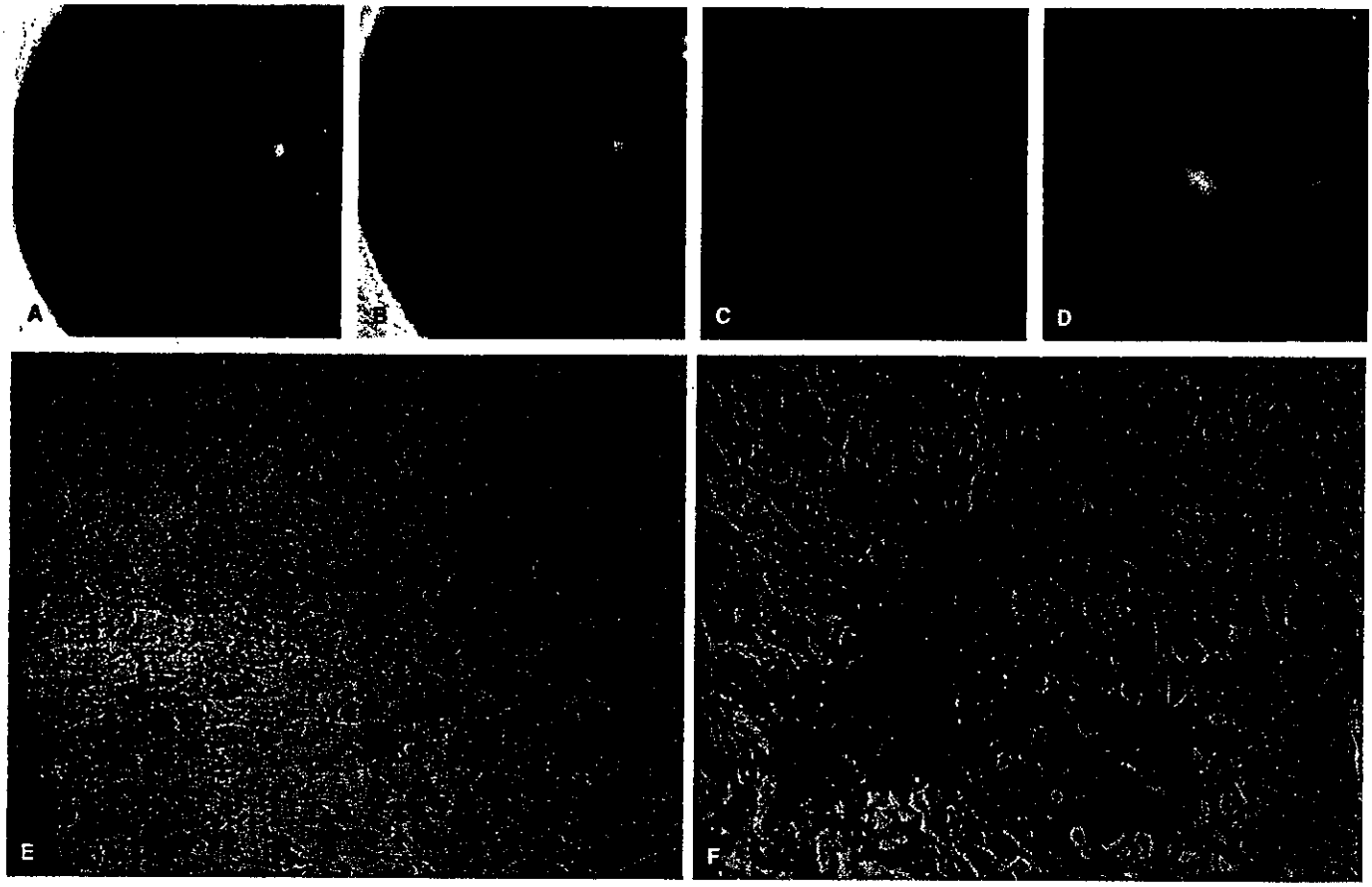

FIGURE 1. Case 1: Adenocarcinoma in a 69-year-old man. A, A faint localized increase in density was identified in segment 1 of the right upper lobe of the lung on a CT screening image obtained in December 2001. B, In retrospect, the opacity was also present on a CT screening image obtained in June 1998. C, Thin-section CT image obtained in December 2001 showing a pGGO in segment 1 of the right upper lobe of the lung. D, Thin-section CT image obtained in June 2002 shows a decrease in the size of the pGGO and the appearance of a solid component. E, Medium-magnification image of the pathologic specimen (H&E staining, ×40). Thickening of the alveolar walls as a result of the tumor cells is visible. F, Medium-magnification image of the pathologic specimen (H&E staining, ×40). Severe narrowing of the alveolar space from the thickening of the alveolar walls and an area of collapse-fibrosis with active fibroblastic proliferation are visible. A right upper lobectomy was performed in January 2003. The lesion was diagnosed as an adenocarcinoma, 17 mm in diameter (Noguchi type C). The size of collapse- fibrosis was 2 mm in diameter.

the natural history of pGGOs after conducting a long-term follow-up study lasting more than 2 years. Five of the 19 cases of pGGOs were diagnosed as lung cancers, that is, 5 BACs (1 case had 2 BACs) and 1 adenocarcinoma, after a mean follow-up of 61 months. Although the patient with adenocarcinoma was followed up for 124 months, personal communication with the author revealed that his lung cancer was of pathologic stage IA and that the size of the central fibrosis of the adenocarcinoma was less than 3 mm in diameter. We have also experienced 2 other pGGOs that developed into mixed GGOs after a 1-year and a 3-year follow-up period, respectively (unpublished data). These lesions were diagnosed as pathologic stage IA adenocarcinomas, and the size of the central fibrosis was 1.5 mm and 2 mm in diameter, respectively. Regarding the relationship between central fibrosis and prognosis, our research team[30] previously reported that 21 out of 100 patients with a lung adenocarcinoma that was 3 cm or less in diameter and which had a central fibrosis of 5 mm or less in diameter had a 5-year survival rate of 100%. Therefore, the adenocarcinoma follow-up cases described above and in this study were thought to be minimally invasive, allowing the possibility of a cure. Third, the adenocarcinoma cases with mixed GGOs did not experience any relapses or deaths, even though the solid components of the GGOs became larger but remained less than 50% of the mixed GGO nodule, this from the standpoint of the GGO's length,[31] the vanishing ratio of GGO[10] ("air-containing type"), and the volume of the GGO.[9] Finally, adenocarcinoma pGGOs tend to grow slowly, as the mean doubling time of pGGOs has been reported to be 813 days[28] or 880 days.[12] In addition, one-fourth of the GGOs in 1 study were

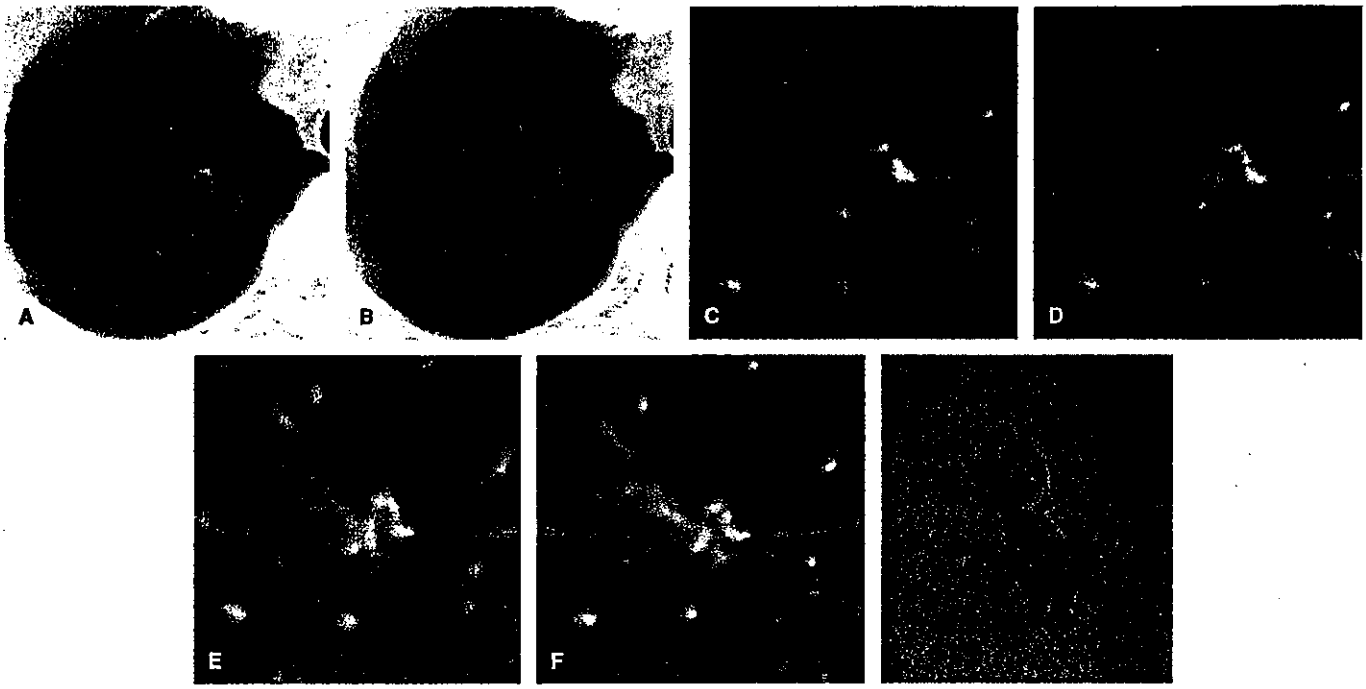

FIGURE 2. Case 2: Bronchioloalveolar carcinoma in a 69-year-old man. A, A faint localized increase in density was identified in segment 1 of the right upper lobe of the lung on a CT screening image obtained in February 1999. B, In retrospect, the opacity was also visible on a CT screening image obtained in February 1998. C, Thin-section CT revealed a pGGO in segment 1 of the right upper lobe of the lung in March 1999. D, Thin-section CT image obtained in February 2000 showing a pGGO with a small solid component. E, Thin-section CT image obtained in February 2001 showing a decrease in the size of the pGGO and a slight increase in the size of the solid component. F, Thin-section CT image obtained in February 2002 showing a larger decrease in the size of the pGGO and an increase in the size of the solid component. G, Low-magnification image of the pathologic specimen (H&E staining, ×5). The foci of alveolar collapse (asterisks) are shown. A right upper lobectomy was performed in May 2002. The lesion was diagnosed as a bronchioloalveolar carcinoma, 15 mm in diameter (Noguchi type B).

stable after a mean follow-up period of 16 months,[17] whereas half of the pGGOs in another study showed no change in size after a median follow-up period of 32 months.[7] Therefore, the classification of some pGGOs may be affected by an overdiagnosis bias.

This study has some limitations. First, the period of pGGO development was not accurately assessed because only thick-sectioned screening CT images were available for the unidentified phase. Therefore, the partial volume effect affected the detectability of small faint opacities on screening CT images. Multislice CT imaging using a narrow collimation and thinner reconstruction images may reveal the natural history of pGGOs more precisely. Second, measurements made with a pair of calipers to calculate doubling times may lead to measurement errors. Although technical advances have been reported,[32,33] we did not have any commercial software for volume measurements. Third, our study cohort was very small. At the start of the helical CT screening project, surgery without follow-up tended to be recommended in cases with pGGO. After knowledge of pGGOs had accumulated (ie, that most pGGOs consisted of preinvasive, noninvasive, or minimally invasive lesions), our treatment procedure changed.[8] Now, resection is only 1 option, not the only option, as in the past. Because of this, resection data cannot always be obtained, and the number of cases was small as a result.

In conclusion, the natural history of pGGOs detected by helical CT screening for lung cancer was partially revealed. A classification for pGGO progression was proposed based on thin-section CT images obtained during the follow-up phase. The pGGOs of lung cancer nodules do not only increase in size or density, but may also decrease rapidly or slowly with the appearance of solid components. Close follow-up until the appearance of a solid component may be a valid option for the management of pGGO.

ACKNOWLEDGMENTS

The authors thank Fumio Shishido, MD, PhD (Department of Radiology, School of Medicine, Fukushima Medical University) for his encouragement. We also wish to thank the pathologists who assisted in this study: Yoshihiro Matsuno, MD (National Cancer Center Research Institute), Tomoyuki Yokose, MD, and Genichiro Ishii, MD (National Cancer Center Research Institute East). We also thank the physicians, the

technical staff, and the administrative staff of the Anti–Lung Cancer Association in Tokyo.

REFERENCES

1. Nakajima R, Yokose T, Kakinuma R, et al. Localized pure ground-glass opacity on high-resolution CT: histologic characteristics. *J Comput Assist Tomogr*. 2002;26:323–329.
2. Nakata M, Saeki H, Takata I, et al. Focal ground-glass opacity detected by low-dose helical CT. *Chest*. 2002;121:1464–1467.
3. Kuriyama K, Seto M, Kasugai T, et al. Ground-glass opacity on thin-section CT: value in differentiating subtypes of adenocarcinoma of the lung. *AJR Am J Roentgenol*. 1999;173:465–469.
4. Yang ZG, Sone S, Takashima S, et al. High-resolution CT analysis of small peripheral lung adenocarcinomas revealed on screening helical CT. *AJR Am J Roentgenol*. 2001;176:1399–1407.
5. Henschke CI, Yankelevitz DF, Mirtcheva R, et al. CT screening for lung cancer: frequency and significance of part-solid and nonsolid nodules. *AJR Am J Roentgenol*. 2002;178:1053–1057.
6. Kodama K, Higashiyama M, Yokouchi H, et al. Prognostic value of ground-glass opacity found in small lung adenocarcinoma on high-resolution CT scanning. *Lung Cancer*. 2001;33:17–25.
7. Kodama K, Higashiyama M, Yokouchi H, et al. Natural history of pure ground-glass opacity after long-term follow-up of more than 2 years. *Ann Thorac Surg*. 2002;73:386–393.
8. Suzuki K, Asamura H, Kusumoto M, et al. "Early" peripheral lung cancer: prognostic significance of ground-glass opacity on thin-section computed tomographic scan. *Ann Thorac Surg*. 2002;74:1635–1639.
9. Matsuguma H, Yokoi K, Anraku M, et al. Proportion of ground-glass opacity on high-resolution computed tomography in clinical T1N0M0 adenocarcinoma of the lung: a predictor of lymph node metastasis. *J Thorac Cardiovasc Surg*. 2002;124:278–284.
10. Kondo T, Yamada K, Noda K, et al. Radiologic-prognostic correlation in patients with small pulmonary adenocarcnomas. *Lung Cancer*. 2002;36:49–57.
11. Austin JM, Muller NL, Friedman PJ, et al. Glossary of terms for CT of the lung: recommendations of the Nomenclature Committee of the Fleischner Society. *Radiology*. 1996;200:327–331.
12. Aoki T, Nakata H, Watanabe H, et al. Evolution of peripheral lung adenocarcinomas: CT findings correlated with histology and tumor doubling time. *AJR Am J Roentgenol*. 2000;174:763–768.
13. White CS, Romney BM, Mason AC, et al. Primary carcinoma of the lung overlooked at CT: analysis of findings in 14 patients. *Radiology*. 1996;199:109–115.
14. Gurney JW. Missed lung cancer at CT: imaging findings in nine patients. *Radiology*. 1996;199:117–122.
15. Koizumi N, Sakai K, Matsuzuki Y, et al. Natural history of cloudy zone of pulmonary adenocarcinoma on HRCT [in Japanese]. *Nippon Igaku Hoshasen Gakkai Zasshi*. 1996;56:715–719.
16. Jang HJ, Lee KS, Kwon OJ, et al. Bronchioloalveolar carcinoma: focal area of ground-glass attenuation at thin-section CT as an early sign. *Radiology*. 1996;199:485–488.
17. Takashima S, Maruyama Y, Hasegawa M, et al. CT findings and progression of small peripheral lung neoplasms having a replacement growth pattern. *AJR Am J Roentgenol*. 2003;180:817–826.
18. Kakinuma R, Ohmatsu H, Kaneko M, et al. Detection failures in spiral CT screening for lung cancer: analysis of CT findings. *Radiology*. 1999;212:61–66.
19. Li F, Sone S, Abe H, et al. Lung cancers missed at low-dose helical CT screening in a general population: comparison of clinical, histopathologic, and imaging findings. *Radiology*. 2002;225:673–683.
20. Kaneko M, Eguchi K, Ohmatsu H, et al. Peripheral lung cancer: screening and detection with low-dose spiral CT versus radiography. *Radiology*. 1996;201:798–802.
21. Sobue T, Moriyama N, Kaneko M, et al. Screening for lung cancer with low-dose helical computed tomography: Anti–Lung Cancer Association project. *J Clin Oncol*. 2002;20:911–920.
22. Schwartz M. A biomathematical approach to clinical tumor growth. *Cancer*. 1961;14:1272–1294.
23. Travis W, Colby T, Corrin B, et al. *Histological Typing of Lung and Pleural Tumors*. Berlin: Springer; 1999.
24. Noguchi M, Morikawa A, Kawasaki M, et al. Small adenocarcinoma of the lung: histologic characteristics and prognosis. *Cancer*. 1995;75:2844–2852.
25. Yankelevitz DF, Henschke CI. Does 2-year stability imply that pulmonary nodules are benign? *AJR Am J Roentgenol*. 1997;168:325–328.
26. Swensen SJ, Jett JR, Hartman TE, et al. Lung cancer screening with CT: Mayo Clinic experience. *Radiology*. 2003;226:756–761.
27. Benjamin MS, Drucker EA, McLoud TC, et al. Small pulmonary nodules: detection at chest CT and outcome. *Radiology*. 2003;226:489–493.
28. Hasegawa M, Sone S, Takashima S, et al. Growth rate of small lung cancers detected on mass CT screening. *Br J Radiol*. 2000;73:1252–1259.
29. Nakata M, Sawada S, Saeki H, et al. Prospective study of thoracoscopic limited resection for ground-glass opacity selected by computed tomography. *Ann Thorac Surg*. 2003;75:1601–1606.
30. Suzuki K, Yokose T, Yoshida J, et al. Prognostic significance of the size of central fibrosis in peripheral adenocarcinoma of the lung. *Ann Thorac Surg*. 2000;69:893–897.
31. Aoki T, Tomoda Y, Watanabe H, et al. Peripheral lung adenocarcinoma: correlation of thin-section CT findings with histologic prognostic factors and survival. *Radiology*. 2001;220:803–809.
32. Yankelevitz Df, Reeves AP, Kostis WJ, et al. Small pulmonary nodules: volumetrically determined growth rates based on CT evaluation. *Radiology*. 2000;217:251–256.
33. Ko JP, Rusinek H, Jacobs EL, et al. Small pulmonary nodules: volume measurement at chest CT-phantom study. *Radiology*. 2003;228:864–870.

Available online at www.sciencedirect.com
SCIENCE DIRECT®
ELSEVIER
Journal of Magnetism and Magnetic Materials 272–276 (2004) e1741–e1742
Journal of magnetism and magnetic materials
www.elsevier.com/locate/jmmm

Wireless micro swimming machine with magnetic thin film

Aya Yamazaki[a,*], Masahiko Sendoh[a], Kazushi Ishiyama[a], Ken Ichi Arai[a], Ryutaro Kato[b], Masaki Nakano[b], Hirotoshi Fukunaga[b]

[a] *Research Institute of Electrical Communication, Tohoku University, 2-1-1 Katahira Aoba-ku, Sendai 980-8577, Japan*
[b] *Nagasaki University, 1-14 Bunkyo-machi, Nagasaki 852-8521, Japan*

Abstract

As the magnetic micro-machines are driven by a magnetic field, they require no power supply cables, no batteries, and no controlling systems on the machine body. We fabricated the spiral-type micro-machine (outer diameter; 0.14 mm, length; 1.0 mm) by a tungsten wire (ϕ 20 μm). NdFeB film magnet was deposited on the spiral-machine by the PLD method. In the experiment, the wireless micro-machine swam at the speed of 0.2–1.6 mm/s. This result indicated that the spiral shape was suitable for miniature swimming machine.

PACS: 85.70.Yv; 85.70.Rp

Keywords: Spiral structure; Magnetic micro-machine; Magnetic thin film; Rotating magnetic field; Reynolds number

1. Introduction

Magnetic micro-machines are driven by a magnetic field. They require no power supply cables, no batteries, and no controlling systems on the machine body. In previous studies, we examined the swimming properties of a spiral-type magnetic micro-machine (outer diameter of 1.5 or 0.8 mm) with the bulk magnet [1,2]. We found that the spiral structure was applicable to swim under a very wide range of Reynolds numbers ($10^{-7} < Re < 10^{3}$), and that the spiral structure was suitable for the miniaturization. However, it is difficult to reduce the size using the bulk magnet. Therefore, we attempted the miniaturization of the micro-machine with magnetic thin film.

2. Magnetic micro-machine

Fig. 1 shows a photograph of the spiral-type magnetic micro-machine. The micro-machine was fabricated with a tungsten wire of a diameter 20 μm. The size of micro-machine has the outer diameter of 0.14 mm and length of 1.0 mm. On the micro-machine, NdFeB film magnet was deposited by the PLD method and thickness of a film was several micros [3]. As the magnet was magnetized in the diameter direction, the machine rotated in synch with the rotating external magnetic field and the spiral structure was generated propellant force.

3. Experiment and analysis result

3.1. Swimming velocity

The spiral-type magnetic micro-machine with thin wire and thin film magnet could swim by the rotating external magnetic field. Fig. 2 shows the relation between the frequency and the swimming velocity of the micro-machine. We used three types of liquids with kinematic viscosity (1, 10, 100 mm^2/s). In Fig. 2, the plots show the experimental results, and the solid line shows the analysis result [4]. The arrow in this graph was the step-out frequency at kinematic viscosity of 100 mm^2/s. At the step-out frequency, the rotation of

*Corresponding author. Tel.: +81-22-217-5488; fax: +81-22-217-5728.
E-mail address: aya@riec.tohoku.ac.jp (A. Yamazaki).

0304-8853/$ - see front matter © 2003 Elsevier B.V. All rights reserved.
doi:10.1016/j.jmmm.2003.12.337

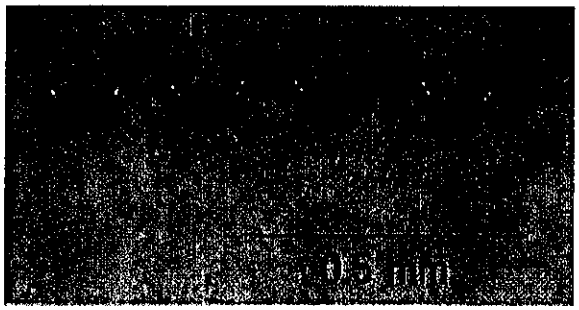

Fig. 1. Photograph of the spiral-type magnetic micro-machine.

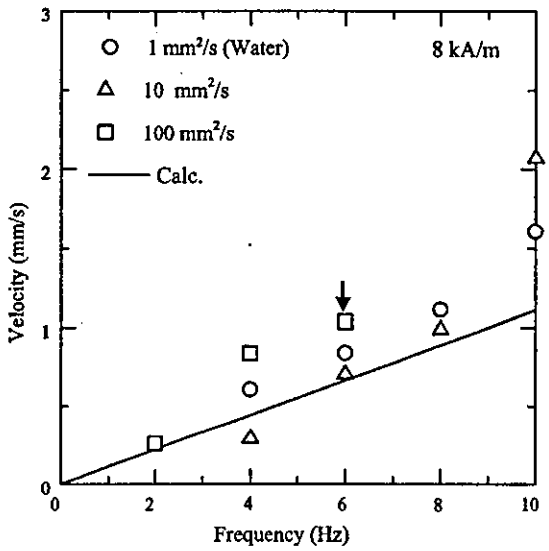

Fig. 2. Relation between frequency and swimming velocity of experimental and analysis.

the machine could not be synchronized to the rotational magnetic field. The micro-machine swam at the speed of 0.2–1.6 mm/s. The Reynolds numbers on this condition were 2×10^{-3}–1.6. This result shows that the spiral shape is suitable for miniature swimming machine.

3.2. Load torque

The value of load torque which the micro-machine receives from the fluid is difficult to obtain by the experiment. However the value of load torque is confirmed by measuring the step-out frequency. At the step-out frequency, the load torque equals to the applied magnetic torque. Therefore, the minimum magnetic field which the micro-machine can rotate was measured at the frequency of the magnetic field of 10 Hz. From this result, the applied magnetic torque was estimated.

Fig. 3 shows the relation between the kinematic viscosity and the torque. The plots show the experimental results of the magnetic torque and the solid line shows the analysis result of load torque [4]. The torque increased with the increase in the kinematic viscosity. In the experiment of swimming velocity, as the magnetic field was 8 kA/m, the step-out frequency was not seen by 1 and 10 mm²/s. In order for the micro-machine to swim, the required magnetic torque is estimated as 10^{-3}–1 nNm and the magnetic field is 0.1–10 kA/m. Therefore, the magnetic torque was very small and the thickness of a magnetic film is realizable by several microns.

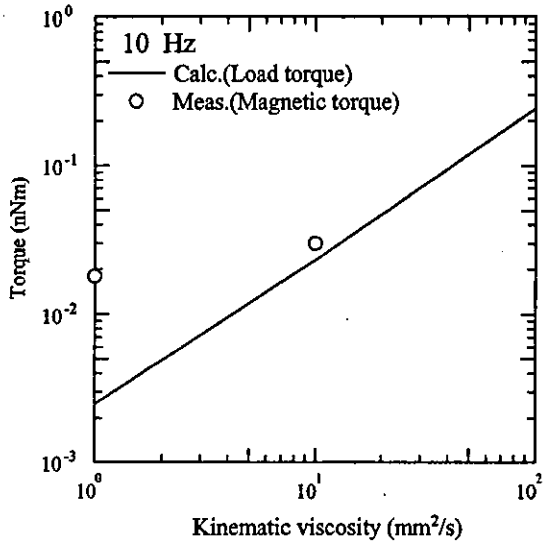

Fig. 3. Relation between kinematic viscosity of liquid and torque.

4. Summary

We fabricated the magnetic micro-machine that was composed of spiral-shaped thin wire and the thin film magnet. The micro-machine with outer diameter 0.14 mm was able to swim wirelessly in the liquids. This result indicated that the spiral shape was suitable for miniature swimming machine. The magnetic torque required for the drive of spiral-type micro-machine was very small, and it was shown that the value could be realized with a magnetic thin film.

References

[1] K. Ishiyama, et al., Sensors and Actuators A 91 (2001) 141.
[2] A. Yamazaki, et al., J. Magn. Soc. Jpn. 27 (2002) 645.
[3] M. Nakano, et al., IEEE Trans, Magn. 38 (2002) 2913.
[4] M. Sendoh, et al., J. Robot. Mec. 12 (2000) 165.

日本応用磁気学会誌 28, 632-635 (2004)

〈論 文〉

らせん型磁気マイクロマシンの泳動特性に対するらせん長の影響

Effect of Machine Length on Swimming Properties of Spiral Magnetic Micro-Machine

山崎彩・仙道雅彦・石山和志・荒井賢一

東北大学電気通信研究所，仙台市青葉区片平 2-1-1（〒980-8577）

A. Yamazaki, M. Sendoh, K. Ishiyama and K. I. Arai

Research Institute of Electrical Communication, Tohoku University, *2-1-1 Katahira Aoba-ku Sendai 980-8577*

In previous studies, we examined a magnetic micro-machine composed a magnet and spiral structure. As the magnet was magnetized in the diameter direction, the micro-machine rotated in synchronism with the rotating magnetic field. This time, we fabricated two types of spiral magnetic micro-machines. One had the magnet and the wire of the spiral structure (head type). The other had the wire of the spiral structure (spiral type). We examined the influence of the micro-machine length. As a result, we found that the swimming velocity of the head type micro-machine depended on the machine length. The swimming velocity of the spiral type micro-machine does not depend on the machine length.

Key words: micro-machine, spiral blade, rotating magnetic field, swimming velocity, machine length

1. はじめに

著者らは，Fig. 1に示すらせん形状に加工したワイヤと磁石から構成される磁気マイクロマシンを開発した[1)2)]．この磁気マイクロマシンは，搭載している磁石が半径方向に着磁されているため，外部から印加される回転磁界に同期して回転する．この磁石の回転がらせん部分で推力に変換され，磁気マイクロマシンは推進する．従って，磁気マイクロマシンは，電源を搭載せず，ワイヤレスでエネルギー供給が可能である．磁気マイクロマシンは，回転磁界面に垂直な姿勢を保ちながら推進を行う．従って，回転磁界面の方向を制御することで，磁気マイクロマシンの推進方向制御をワイヤレスで行うことが可能となる[3)]．

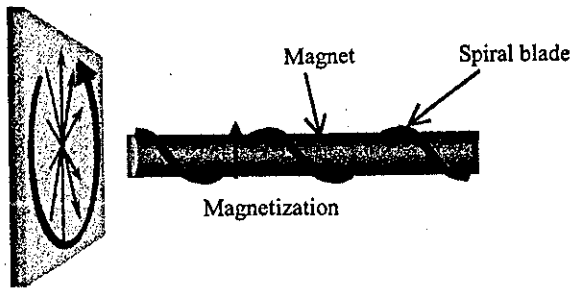

Fig. 1 Schematic view of magnetic micro-machine.

らせん型マイクロマシンの形状を決める要素として，マシンの直径，マシンの長さ，らせん形状がある．これらの要素が泳動特性に与える影響を検討し，駆動に必要な磁気トルク，効率の良い形状について検討し，マシン設計を行う必要がある．我々は先の研究において，有限体積法を用いた流体力学的泳動特性解析手法を確立し，マシン直径が0.15～1.5 mmの磁気マイクロマシンについて，実験と解析から泳動特性の検討を行った．その結果，らせん構造の磁気マイクロマシンは，レイノルズ数が10^{-7}～10^{3}と幅広い条件下で駆動することができ，らせん構造が小形化に適した構造であることを示してきた[4)5)]．らせんの高さ，角度の変化による泳動特性への影響について検討を行い，らせん形状に関する設計指針が得られた[5)6)]．

本研究では，これまでに検討を行っていないマシンの長さによる泳動特性の影響について実験と解析から検討を行った．解析には，先の研究で確立した有限体積法を用いた3次元泳動特性解析手法[7)]を用いて行った．

2. 磁気マイクロマシン

Fig. 2 (a)，Fig. 2 (b) に検討を行った2種類の磁気マイクロマシンの写真を示す．Fig. 2 (a)のマシンは，半径方向に着磁されたSmFeN磁石(φ 1.2×0.55 mm)とらせん形状に加工した直径0.15 mmのタングステンワイヤから構成されており，以後Head型マイクロマシンと呼ぶ．このマシンのらせんピッチは4.4 mmである．Fig. 2 (b)は，直径20 μmのタングステンワイヤをらせんピッチ0.2 mmで加工したマシン(Spiral型マイクロマシン)である．ワイヤ表面にPLD (Pulsed Laser Deposition) 法[8)]を用いて，NdFeB薄膜磁石を数μm積層した．磁化方向は半径方向である．

3. 実験と解析結果

3.1 Head型マイクロマシン

Head型マイクロマシンの実験では，動粘度 1×10^{4} mm²/sのシリコーンオイルで満たされた試験管内にマシンを挿入した．外部から12 kA/m (150 Oe)の回転磁界を印

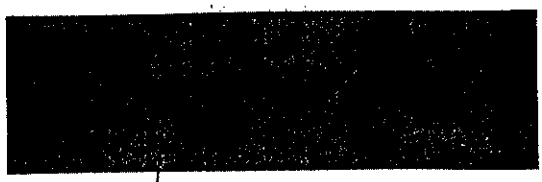

(a) Head type magnetic micro-machine.

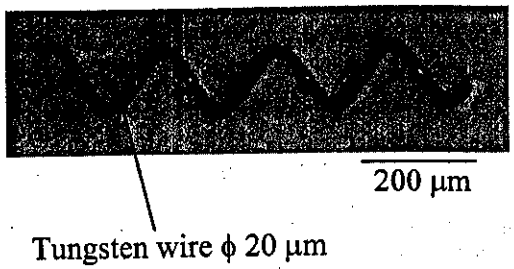

(b) Spiral type magnetic micro-machine.

Fig. 2 Photograph of magnetic micro-machine.

加し，Head 型マイクロマシンの泳動速度の測定を行った．回転磁界周波数は 1 Hz とした．Fig. 3 に Head 型マイクロマシンの泳動速度の実験と解析結果を示す．プロットに実験結果，実線に有限体積法を用いた 3 次元泳動特性解析の結果を示す．Head 型マイクロマシンは，マシン長さ L の減少により，泳動速度は遅くなり，L の増加につれて泳動速度は増加し飽和する結果が得られた．実験において，マシン長さ L が長い時，磁石部分が下がり傾いた状態で推進するのが確認された．この影響により L が長くなると実験値と解析値の誤差が大きくなったと考えられる．

Fig. 4 にマシンが流体から受ける抵抗力についての解析結果を示す．破線はらせん部分で受ける抵抗力，一点鎖線は磁石部分で受ける抵抗力，実線はマシン全体の抵抗力である．ここで，マシンが流体から受ける抵抗力は，らせん，磁石のそれぞれに作用するせん断力である．せん断力の式を(1)式に示す[9]．

$$\begin{aligned} D &= S.F \\ &= \tau \cdot A \\ &= \mu \cdot v \cdot A \end{aligned} \qquad (1)$$

D: Drag [N]
$S.F$: Shearing force [N]
τ: Shearing stress [N/m^2]
A: Area [m^2]
μ: Coefficient of viscosity [N s/m^2]
v: Rate of shearing deformation [1/s]

らせん部分で受ける抵抗力は，L の増加に伴い表面積が増

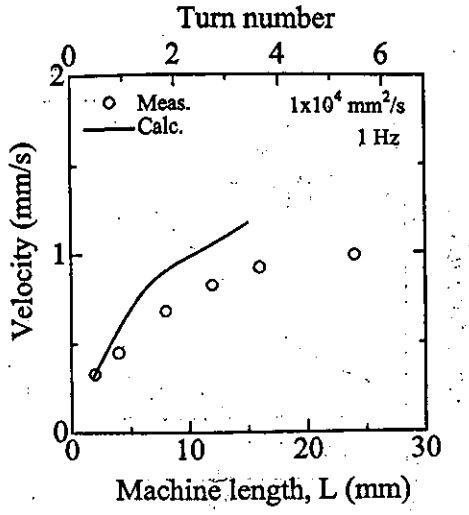

Fig. 3 Relation between swimming velocity and length of the experimental machine and analysis results (Head type).

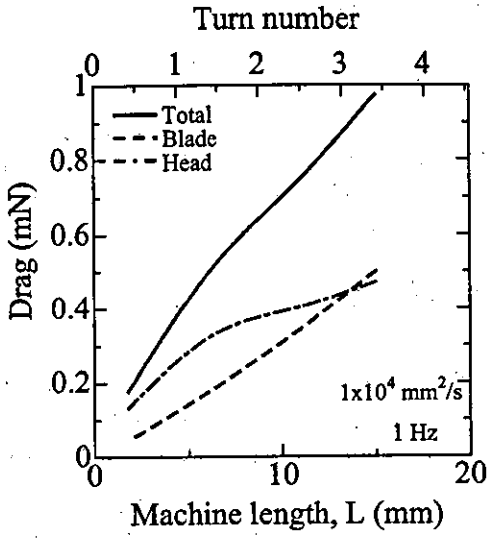

Fig. 4 Relation between drag and length of the machine of the analysis results (Head type).

加するため，増加する．磁石部分で受ける抵抗力は，L が短い時，らせん部分で発生する推力に対して大きくなる．このため，泳動速度が減少したと考えられる．従って，泳動速度の減少により，磁石部分で受ける抵抗力が減少したと考えられる．一方，L が長いときは，らせん部分で発生する推力に対して磁石部分で受ける抵抗力の影響は小さく，泳動速度が飽和したと考えられる．従って，磁石部分で受ける抵抗力は，一定値に飽和した．

Fig. 5 にマシンが流体から受ける負荷トルクと L の関係を示す．一点鎖線と破線はそれぞれらせん部分のせん断応力と圧力に起因するものである．二点鎖線は磁石部分のせん断応力に起因する負荷トルクを示す．せん断力による負荷トルクは，せん断力と回転中心からの距離の積であらわ

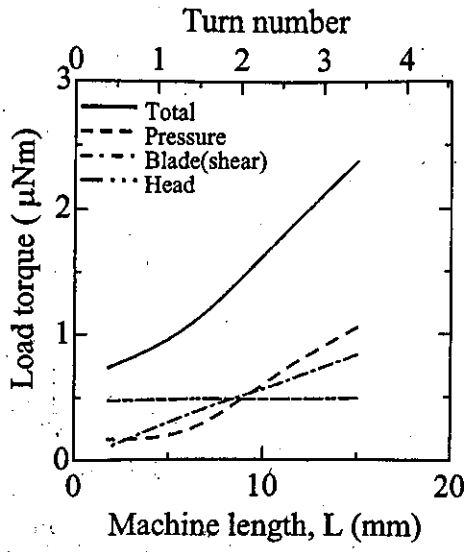

Fig. 5 Relation between load torque and length of the machine of the analysis results (Head type).

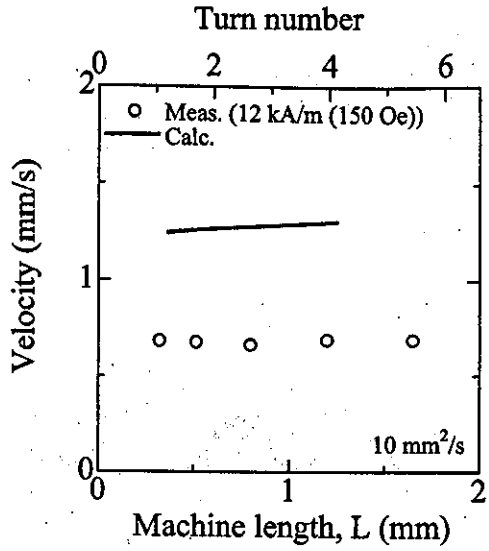

Fig. 6 Relation between swimming velocity and length of the experimental machine and analysis results (Spiral type).

される．磁石で受ける負荷トルクは，Lの長さによらずせん断力は一定であるため，負荷トルクの値も一定値である．らせん部分の負荷トルクは，Lの増加とともに表面積が増加するため，負荷トルクも増加する．従って，全体の負荷トルクは，Lの増加に伴い増加する．

3.2 Spiral型マイクロマシン

Spiral型マイクロマシンの実験は，動粘度10 mm²/sのシリコーンオイルで満たされた幅1.6 mmの流路内で行った．印加磁界強度8 kA/m (100 Oe)，回転磁界周波数10 Hzの時の泳動速度を測定した．Fig. 6にSpiral型マイクロマシンの長さに対する泳動速度の解析と実験結果を示す．プロットは実験の結果，実線は解析の結果を示す．実験と解析の結果，どちらもLの値によらず泳動速度は一定値であるが，値の大きさにずれが生じた．これは，実験において，マシンが流路の底に沈んだ状態で泳動しているのに対し、解析でのマシンと流路の位置は十分離れた状態にある。従って、解析には含まれない摩擦による影響が原因であると考えられる．

Fig. 7にSpiral型マイクロマシンの長さに対する流体から受ける抵抗力の関係を示す．Spiral型マイクロマシンはらせん部分のみで抵抗力が発生するため，抵抗力はLに比例して増加した．

Fig. 8にSpiral型マイクロマシンの長さに対する流体から受ける負荷トルクの関係を示す．一点鎖線と斜線は，それぞれらせん部分で受けるせん断応力と圧力による負荷トルクの解析結果を示す．実線にマシン全体の負荷トルクの解析結果を示す．解析の結果，Lの増加とともに，負荷トルクは増加した．

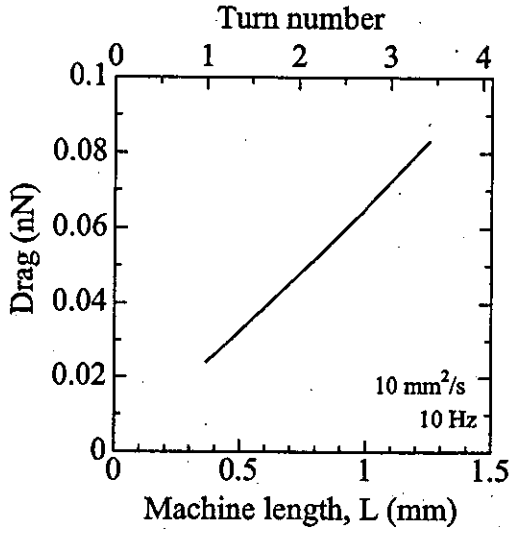

Fig. 7 Relation between drag and length of the machine of the analysis results (Spiral type).

3.3 流体力学的効率

泳動時，マシンが流体に対してなすパワーのうち，推進に使われるパワーの比を流体力学的効率 ε として(2)式のように定義し，特性を評価するパラメータの一つとした．

$$\varepsilon = \frac{\text{推進速度}\times\text{推力}}{\text{推進速度}\times\text{推力}+\text{角速度}\times\text{負荷トルク}} \quad (2)$$

Fig. 9 に，らせんのターン数に対する流体力学的効率を示す．実線に，Head 型マイクロマシン，破線に Spiral 型マイクロマシンの解析結果を示す．Head 型マイクロマシンは，らせんのターン数が小さい時，効率は小さく，らせんのターン数が大きくなる時，効率は大きくなり，飽和する結果が得られた．3.1 から，Head 型マイクロマシンはらせんのターン数が小さい(マシンの長さが短い)場合は，磁石の影響を大きく受けるということに起因していると考えられる．従って，らせんのターン数は多すぎても，効率は変わらず，負荷トルクだけが大きくなるため，負荷が小さく，効率の良いマシンを得るためには，らせんのターン数は，2 ターンであることがわかる．Spiral 型マイクロマシンは，らせんのターン数が少ない時，効率がよく，らせんのターン数の増加とともに，効率は減少する．従って，効率の良い Spiral 型マイクロマシンは，らせんのターン数を少ない方が良い．

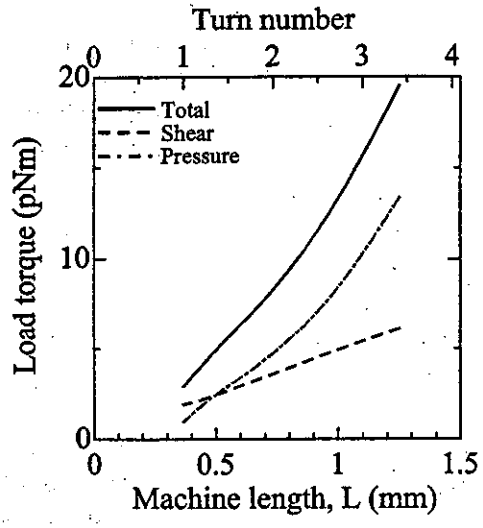

Fig. 8 Relation between load torque and length of the machine of the analysis results (Spiral type).

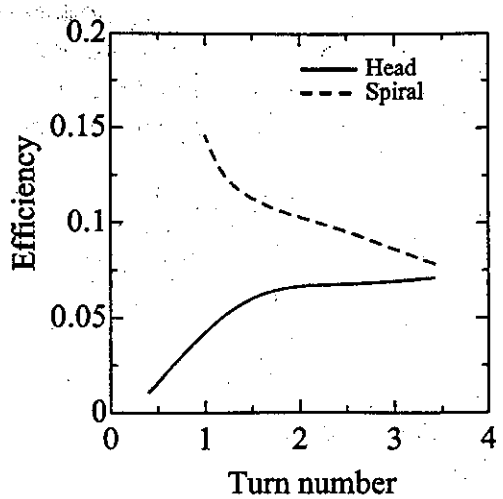

Fig. 9 Relation between efficiency and turn number of the spiral of the analysis results.

4. まとめ

2 種類の磁気マイクロマシンを作製した．ひとつは，磁石とワイヤから構成される Head 型マイクロマシン，もうひとつは，ワイヤから構成される Spiral 型マイクロマシンである．2 種類のマイクロマシンの長さを変えて，マシンの長さによる泳動特性の影響を実験と解析から検討を行った．その結果，Head 型マイクロマシンは，L の大きさに依存する結果が得られた．さらに，効率がよく，負荷トルクの小さくなる L の大きさは，らせんのターン数は，2 ターンである結果が得られた．Spiral 型マイクロマシンの泳動速度は，L によらず一定値である結果が得られた．効率の良いマシンは，L を短くした方が良いという結果が得られた．

謝辞

Spiral 型マシン作製の際，PLD 法による NdFeB 磁石の製膜をして頂いた，長崎大学の福永教授，中野助手に感謝します．

本研究の一部は「21 世紀 COE 新世代情報エレクトロニクスシステムの構築」により行ったものです．関係者各位に感謝します．

文　献

1) M. Sendoh, N. Ajiro, K. Ishiyama, M. Inoue and K. I. Arai, IEEE Transactions on Magnetics, 36, 3688 - 3690, 1999.
2) K. Ishiyama, M. Sendoh, A. yamazaki, K. I. Arai, Sensors and Actuators A 91, 141-144, 2001.
3) M. Sendoh, A. Yamazaki, K. Ishiyama, K. I. Arai, T. Inoue, Transaction IEE of Japan, 120-A, 301-306, 2000.
4) K. Ishiyama, M. Sendoh, A. Yamazaki, M. Inoue, K. I. Arai, IEEE Transactions on Magnetics, 37, 2868 - 2870, 2001.
5) M. Sendoh, N. Ajiro, K. Ishiyama, M. Inoue T. Hayase and K. I. Arai, Journal of Robotics and Mechatronics 12, 165-171, 2000.
6) A. Yamazaki, M. Sendoh, K. Ishiyama, T. Hayase, K. I. Arai, Journal Magnetic Society of Japan 27, 645-648, 2002.
7) A. Yamazaki , M. Sendoh , K. Ishiyama , K. I. Arai , T. Hayase, Sensors and Actuators A 105-1 103-108.
8) M. Nakano, S. Tsutsumi, H. Fukunaga, IEEE Transaction on Magnetics, 38, 2913-2915, 2002.
9) T. Ikui, M, Inoue, "Dynamics of viscous fluid", Rikogakusha, Tokyo, p. 4, 1978.

2003 年 10 月 27 日受理，2004 年 1 月 15 日採録

The British Journal of Radiology, 77 (2004), 787–789 © 2004 The British Institute of Radiology
DOI: 10.1259/bjr/93367963

Case report

Cervical oesophageal stent placement via a retrograde transgastric route

[1]Y INABA, MD, [2]M KAMATA, MD, [1]Y ARAI, MD, [1]K MATSUEDA, MD, [1]T ARAMAKI, MD and [1]H TAKAKI, MD

Departments of [1]Diagnostic and Interventional Radiology and [2]Radiation Oncology, Aichi Cancer Center, 1-1 Kanokoden Chikusa-ku, Nagoya 464-8681, Japan

Abstract. During attempted oesophageal stent placement in a patient with cervical oesophageal cancer in whom swallowing of even saliva was impossible, transoral access to the cervical oesophagus was unsuccessful. Under ultrasound and fluoroscopy guidance, percutaneous gastric puncture was performed, and using an angiographic catheter and guidewire, access to the oesophagus by a retrograde transgastric route was successfully achieved. The obstructed segment of the oesophagus was traversed. It was then possible to pull the guidewire through the mouth and place an oesophageal stent via an antegrade approach.

The usefulness of metallic stents for the palliation of malignant oesophageal stenoses is well established [1–3]. In general, stent placement in the oesophagus begins with the transoral passage of a guidewire through the oesophageal stenosis under endoscopic or fluoroscopic guidance. Cases are occasionally encountered in which passage of the guidewire is made difficult by the severity of the stenosis. By utilizing angiographic techniques with catheters and guidewires, impassable oesophageal stenoses have become rare.

We recently encountered a patient in whom even swallowing saliva was impossible. Transoral access to the distal cervical oesophagus was not possible due to the severity of the stenosis. As such, we performed a percutaneous gastric puncture, and gained access to the oesophagus by a retrograde transgastric route. It was then possible to pass the guidewire through the stricture into the mouth and place an oesophageal stent via a transoral route antegradely.

Case report

A 55-year-old man with cervical oesophageal cancer associated with tracheal invasion, was treated with external beam radiotherapy (72 Gy) combined with chemotherapy (5-FU and nedaplatin). From the start of these treatments, swallowing of liquids became impaired, and intravenous hyperalimentation was administered. After this treatment the invaded tracheal portion showed improvement, but the patient's dysphagia worsened, and even the swallowing of saliva became impossible. Unfortunately a nasogastric tube for feeding could not be inserted, and under ultrasound guidance the gastric wall was percutaneously punctured with a 23 G needle, the stomach inflated by injecting air into the gastric lumen, and percutaneous gastric puncture performed once again under fluoroscopic guidance using a Cope gastrointestinal suture anchor set (Cook, Bloomington, IN) to create a gastrostomy. However, 1 month later the gastrostomy tube was removed because of a subcutaneous infection around the gastrostomy site.

It was decided to insert an oesophageal self-expanding metallic endoprosthesis, and the cervical oesophagus was approached transorally. Using an angiographic catheter and guidewire, passage through the obstructed portion of the oesophagus was attempted, but the guidewire only entered the associated oesophagotracheal fistula (Figure 1) and did not reach the proximal side of the oesophagus. Endoscopic attempts to traverse the obstruction were also unsuccessful. After treatment of the subcutaneous infection at the earlier gastrostomy site, a repeat percutaneous gastric puncture under ultrasound and fluoroscopy guidance was performed, and a 5 F angiographic sheath (Terumo, Tokyo, Japan) placed in the stomach. An angiographic catheter (5 F Headhunter; Clinical Supply, Gifu, Japan) and guidewire (0.035″ Radifocus; Terumo, Tokyo, Japan) were used to retrogradely cannulate the oesophageal stricture (Figure 1). The guidewire and catheter were then pulled through the mouth. The guidewire was then exchanged for a stiff wire 0.035″ Zebra exchange guidewire (Microvasive/Boston Scientific, Natick, MA). A 24 F Teflon sheath (Cook) was inserted in a transoral, antegrade fashion distal to the oesophageal obstruction, and a covered oesophageal stent (10 cm long covered Ultraflex; Microvasive/Boston Scientific) released proximally, and positioned under fluoroscopy such that its proximal edge did not extend as far as the oral side of the orifice of the oesophagus (Figure 2). The upper edge of the stent after placement was located at the level of the centre of the C6 vertebral body. A nasogastric tube was inserted, and the sheath placed in the stomach was removed. After stent placement the patient felt neither cervical pain nor foreign-body sensation, but experienced pain when attempting to swallow saliva. A follow up contrast study performed on the 4th day after stent placement, showed the stent to be almost completely expanded, and the associated shortening of its long axis resulted in a slightly

Received 9 September 2003 and in revised form 8 December 2003, accepted 3 February 2004.

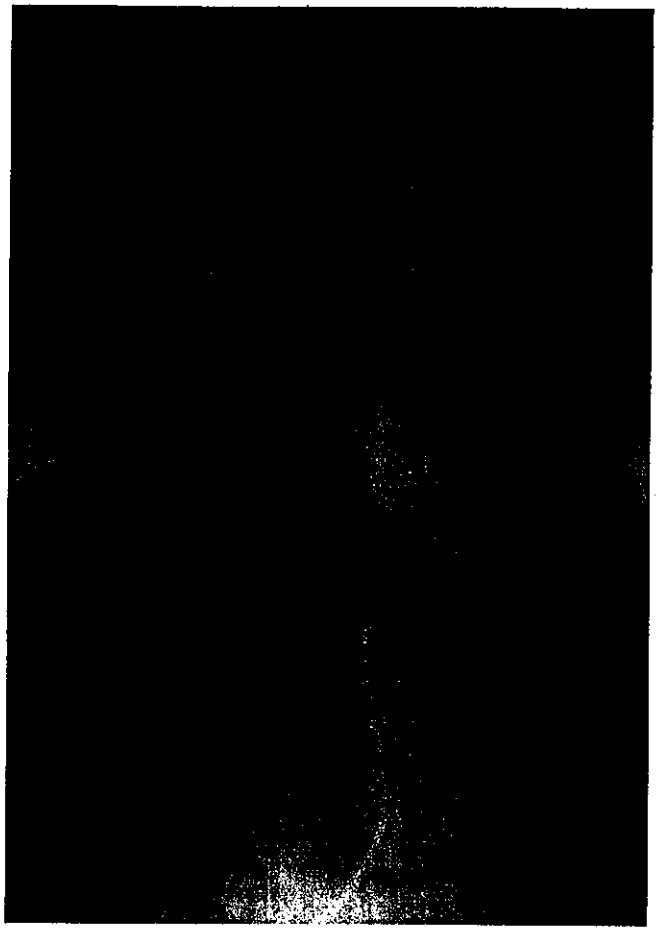

Figure 1. Contrast oesophogogram performed retrogradely via the catheter inserted from the stomach and positioned at the distal edge of the obstructed portion of the oesophagus (arrows). The oesophagus proximal to the stricture and an oesophagotracheal fistula (arrowheads) are visualized.

lower position of the upper edge of the stent. Although only a small volume of contrast material could be swallowed at a time, passage through the stented area was good, and no oesophagotracheal fistula was depicted.

7 days after stent placement the patient was able to swallow smoothly, and oral ingestion of semi-solids became feasible, allowing removal of the nasogastric tube. He died of progressive cancer 5 months after the stent placement, with oral intake continuing to be possible up to the week prior to his death.

Discussion

The use of expandable metallic stents for oesophageal stenoses due to unresectable malignant tumours is now established as valuable palliation, with the rapid amelioration of symptoms in a high proportion of cases. It is minimal invasive and low risk [1–3]. Stent placement is usually possible from the cervical oesophagus to oesophagogastric junction. In the cervical oesophagus there is concern that the more proximally the stent is placed the more marked will be the foreign-body sensation felt by the patient [1]. For this reason, initially stent placement near the oesophageal orifice (within 2 cm of the cricopharyngeus) was considered to be contraindicated [1].

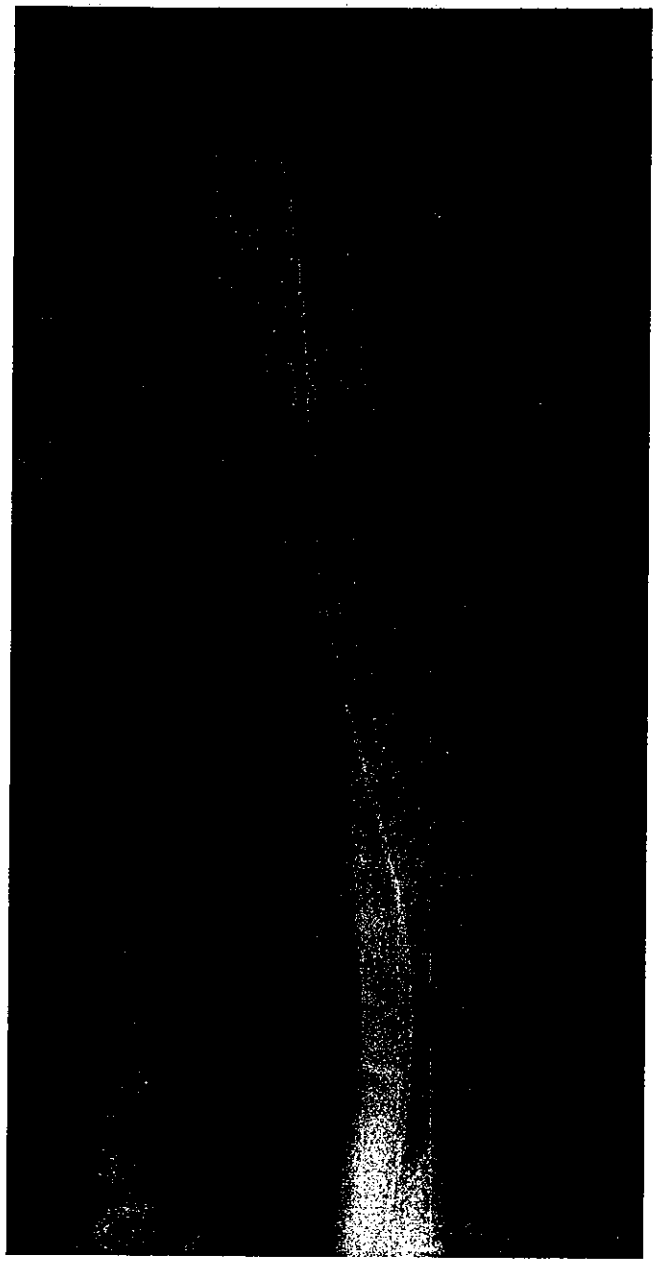

Figure 2. The oesophageal stent inserted via a transoral, antegrade fashion is seen at the level of the oesophageal stricture.

Recently there have been some reports noting an absence of foreign-body sensation problems with stent placement up to the cricopharyngeus [4–7].

Stent placement in the oesophagus is usually via the transoral passage of a guidewire under endoscopic or fluoroscopic guidance through the stenotic portion of the oesophagus. Even in cases in which the severity of the stenosis precludes easy passage, this can usually be achieved by using angiographic technique with angiographic catheters and hydrophilic guidewires. Hitherto we had never experienced a case in which we had to abandon such a procedure because of the unsuccessful passage of a guidewire through the stenosis.

However, in the patient with cervical oesophageal cancer we describe, it was not possible to pass a guidewire transorally through the obstructed portion of the oesophagus. The distance from the cricopharyngeus to the

obstructed portion was approximately 3 cm. Since the radiochemotherapy treatment had successfully reduced the size of the infiltrated portion of the trachea, it is possible that rather than progression of the cancer itself, marked fibrosis associated with the radiotherapy developed.

In cases of vascular obstruction it is not unusual if passage of a guidewire from one direction is difficult, to be able to pass the guidewire from the opposite direction with relative ease [8]. A transgastric retrograde approach was attempted making use of percutaneous gastrostomy technique, and as the stomach was collapsed ultrasound guidance was used. The oesophageal obstruction was traversed retrogradely, enabling a stent to be placed at the stricture. Before the present case, Novak et al reported percutaneous transgastric placement of oesophageal stents [9]. They inserted the 18–24 F delivery system through a gastrostomy, while we placed a 5 F angiographic sheath only in the stomach and pulled a guidewire retrogradely through the mouth, and then inserted the delivery system via an oral route antegradely. After stent placement the 5 F sheath via a transgastric route was removed, but no complications occurred.

Although it is unclear how effective a retrograde approach can be for luminal obstruction when passage from one direction is difficult, in cases in which access can be achieved an approach from both sides should be considered.

References

1. Song HY, Do YS, Han YM, et al. Covered, expandable esophageal metallic stent tubes: experiences in 119 patients. Radiology 1994;193:689–95.
2. Inaba Y, Arai Y, Takeuchi Y, et al. Treatment of malignant gastrointestinal stenoses with expandable metallic stents. J Jpn Soc Angiography Interv Radiol 1997;12:363–9.
3. Siersema PD, Hop WC, van Blankenstein M, et al. A comparison of 3 types of covered metal stents for the palliation of patients with dysphagia caused by esophagogastric carcinoma: a prospective, randomized study. Gastrointest Endosc 2001;54:145–53.
4. Segalin A, Granelli P, Bonavina L, Siardi C, Mazzoleni L, Peracchia A. Self-expanding esophageal prosthesis. Effective palliation for inoperable carcinoma of the cervical esophagus. Surg Endosc 1994;8:1343–5.
5. Bethge N, Sommer A, Vakil N. A prospective trial of self-expanding metal stents in the palliation of malignant esophageal strictures near the upper esophageal sphincter. Gastrointest Endosc 1997;45:300–3.
6. Conio M, Caroli-Bosc F, Demarquay JF, et al. Self-expanding metal stents in the palliation of neoplasms of the cervical esophagus. Hepatogastroenterology 1999;46:272–7.
7. Macdonald S, Edwards RD, Moss JG. Patient tolerance of cervical esophageal metallic stents. J Vasc Interv Radiol 2000;11:891–8.
8. Takeuchi Y, Arai Y, Kasahara T, Inaba Y, Shindo J, Kumada T. Technical aspects of venous stenting in high-grade stenoses using a long guidewire between dual venous access sites. Eur Radiol 2000;10:167–9.
9. Novak Z, Coldwell DM, Mitchell RD, Ryu RK, Kandarpa K. Percutaneous transgastric placement of esophageal stents. J Vasc Interv Radiol 1999;10:428–30.

Primary Mediastinal Lymphoma

Characteristic Features of the Various Histological Subtypes on CT

Ukihide Tateishi, MD, PhD, Nestor L. Müller, MD, PhD,† Takeshi Johkoh, MD, PhD,‡ Yasushi Onishi, MD,§ Yasuaki Arai, MD, PhD,* Mitsuo Satake, MD,* Yoshihiro Matsuno, MD, PhD,‖ and Kensei Tobinai, MD, PhD§*

Objective: To assess the characteristic features of the primary mediastinal lymphoma (PML) on CT and to test the relationship between CT findings and the likelihood of the 3 most common subtypes (Hodgkin lymphoma [HL], mediastinal diffuse large B-cell lymphoma [Med-DLBCL], and precursor T-cell lymphoblastic lymphoma [T-LBL]).

Methods: Sixty-six consecutive patients with pathologically proven PML including 29 patients with HL, 21 with Med-DLBCL, and 16 with T-LBL underwent CT prior to therapy. CT scans were independently reviewed by 2 radiologists who were blinded to the pathologic diagnosis for the following considerations: pattern of involvement (i.e., morphologic features, mass size, and contrast enhancement pattern), and ancillary findings at other sites including neck, abdomen, and pelvis. Interobserver agreement was measured by Kappa statistics, and independent predictors were calculated using multiple logistic regression analysis for determining the likelihood of the subtypes based on CT.

Results: Characteristic features of HL included irregular contour of the anterior mediastinal mass (20 of 29, 69%) and high prevalence of associated mediastinal lymphadenopathy (28 of 29, 97%). Characteristic features of Med-DLBCL included regular contour (14 of 21, 67%) and absence of cervical and abdominal lymphadenopathy (0 of 21). Characteristic features of T-LBL included regular contour (12 of 16, 75%) and high prevalence of cervical (9 of 16, 56%) and abdominal (6 of 16, 38%) lymphadenopathy and splenomegaly (11 of 16, 69%). CT findings independently associated with increased likelihood of HL were surface lobulation ($P < 0.01$), the absence of vascular involvement ($P < 0.01$), or pleural effusion ($P < 0.05$). The presence of vascular involvement was associated with increased likelihood of Med-DLBCL ($P < 0.001$). Furthermore, CT findings including the presence of cervical lymph nodes or inguinal lymph nodes ($P < 0.001$), the presence of pericardial effusion ($P < 0.05$), and the absence of surface lobulation ($P < 0.05$) were significantly associated with the likelihood of T-LBL.

Conclusion: The various histologic subtypes of PML have characteristic manifestations in the neck, chest, and abdomen, which allow their distinction on CT.

Key Words: malignant lymphoma, mediastinal tumor, computed tomography

(*J Comput Assist Tomogr* 2004;28:782–789)

Malignant lymphoma that involves mainly or exclusively the mediastinum at initial presentation (primary mediastinal lymphoma: PML) is a relatively common condition seen in patients of all ages.[1–4] Most cases are due to 1 of 3 histologic subtypes: Hodgkin lymphoma (HL), mediastinal diffuse large B-cell lymphoma (Med-DLBCL), and precursor T-cell lymphoblastic lymphoma (T-LBL). Distinction of the specific histologic subtype is important as it influences treatment and prognosis.[5–12] Because the specific diagnosis should be confirmed by immunohistochemical analysis and hence requires large tissue samples, it is not always easy to make a confident diagnosis on biopsy specimens.[7–10]

There is a sizable body of literature examining the distribution of nodes or masses in lymphoma.[13–27] However, there is limited information on the characteristic manifestations of the various subtypes of PML and the potential value of CT in the differential diagnosis. CT has been increasingly used for the evaluation of patients with suspected or proven lymphoma. It allows for accurate staging of the disease and follow-up of the therapeutic response.[15–23] The purpose of the present study was to assess the characteristic features of the various histologic subtypes of PML and the diagnostic accuracy of CT evaluation for a specific histologic subtype.

MATERIALS AND METHODS

Patients

Sixty-six cases of PML were registered in the radiologic files of our institute. Clinical details and follow-up information including the presence or absence of recurrence were reviewed retrospectively by a hematologic oncologist who was one of the authors. Our institutional review board does not require its approval or patient informed consent for this type of review. The study included 45 men (mean age 38.4 years, range 16 to 84 years) and 21 women (mean age 34.1 years, range 13 to 63 years). All patients underwent uniform staging that included a physical examination, blood cell counts, routine blood

From the *Division of Diagnostic Radiology, National Cancer Center Hospital, Tokyo, Japan; †Division of Hematologic Oncology, National Cancer Center Hospital, Tokyo, Japan; ‖Division of Pathology, National Cancer Center Hospital, Tokyo, Japan; §Department of Radiology, University of British Colombia and Vancouver Hospital and Health Sciences Centre, Canada; and ‡Department of Medical Physics, Osaka University Graduate School of Medicine, Osaka, Japan.

Reprints: Ukihide Tateishi, MD, PhD, Division of Diagnostic Radiology, National Cancer Center Hospital, Tsukiji, Chuo-Ku, 104-0045, Tokyo, Japan (E-mail: utateish@ncc.go.jp).

chemistries, and bone marrow aspiration. Clinical features, International Prognostic Index (IPI) scores,[28] and clinical stages were recorded.

Histopathologic confirmation of definite diagnosis in all patients was obtained by core needle or excisional biopsy. Biopsy sites included the anterior mediastinal mass in 33 patients, cervical lymph node in 25, and both in 8. Fifty-four patients (82%) were confirmed by the initial biopsy alone and the other 12 patients (18%) underwent subsequent biopsy because of insufficient initial sample.

Immunohistochemical studies to determine histologic subtype were performed in all biopsy specimens. According to a recent classification system[29] devised by the World Health Organization (WHO), 29 patients had classic HL, 21 had Med-DLBCL, and 16 had T-LBL. The presence or absence of nodal involvement in each suspected lesion was determined at biopsy in 36 sites and the remaining with a combination of imaging findings and clinical follow-up. Extranodal involvement in the abdomen confirmed by endoscopic, needle, or excisional biopsy included stomach (n = 1), kidney (n = 1), and spleen (n = 1).

The histopathologic findings were reviewed by an experienced pathologist who was one of the authors. Chart, review of histologic specimens, and patient file reviews were

TABLE 1. CT Findings in Patients With PML and the Other Common Nonlymphomatous Diseases

Disease	PML	Thymoma	Thymic cancer	GCT	SCLC
No. of patients	66	19	26	13	12
Male/female	45/21	8/11	18/8	13/0	9/3
Age (mean ± SD) (y)	37.0 ± 14.9	55.6 ± 12.2	58.4 ± 11.6	26.5 ± 5.4	64.5 ± 8.3
Age range (y)	13–84	29–74	24–74	18–38	51–78
Tumor margins*					
Well-defined margins	39 (59)	18 (95)	22 (85)	1 (8)	0
Ill-defined margins	27 (41)	1 (5)	4 (15)	12 (92)	12 (100)
Size of main mass (mean ± SD) [cm]	8.9 ± 3.0	5.2 ± 1.8	7.2 ± 2.4	11.6 ± 2.2	5.6 ± 1.6
Presence of surface lobulation	31 (47)	7 (37)	19 (73)	0	12 (100)
Presence of vascular encasement	21 (32)	1 (5)	20 (77)	7 (54)	2 (17)
Presence of chest wall invasion	10 (15)	0	13 (50)	3 (23)	0
Presence of cutaneous involvement	3 (5)	0	0	0	0
Presence of lung invasion†	11 (17)	0	0	0	NA
Presence of nodal involvement					
Cervical lymph node (superficial)†	10 (15)	0	0	0	0
Cervical lymph node (deep)§	18 (27)	0	0	0	0
Submandibular lymph node	1 (2)	0	0	0	0
Submental lymph node	2 (3)	0	0	0	0
Parotid lymph node	2 (3)	0	0	0	0
Supraclavicular lymph node	11 (17)	0	0	0	10 (83)
Mediastinal lymph node§	50 (76)	0	12 (46)	1 (8)	12 (100)
Hilar lymph node†	12 (15)	0	2 (8)	2 (15)	12 (100)
Axillary lymph node§	12 (15)	0	0	0	0
Celiac lymph node	4 (6)	0	0	0	0
Paraaortic lymph node§	12 (15)	0	0	0	0
Mesenteric lymph node	2 (3)	0	0	0	0
Iliac lymph node	1 (2)	0	0	0	0
Inguinal lymph node*	5 (8)	0	0	0	0
Presence of pleural effusion	26 (39)	2 (10)	8 (31)	5 (38)	5 (42)
Presence of pericardial effusion*	24 (36)	0	4 (15)	3 (23)	3 (25)
Hepatomegaly	2 (3)	0	0	0	0
Splenomegaly§	13 (20)	0	0	0	0
Presence of metastasis					
Lung metastasis§	0	0	5 (19)	7 (54)	3 (25)
Liver metastasis§	0	0	1 (4)	1 (8)	5 (42)
Splenic metastasis	1 (2)	0	0	1 (8)	0
Adrenal metastasis	0	0	0	0	1 (8)
Presence of pleural dissemination	13 (20)	2 (10)	6 (23)	2 (15)	2 (17)

Data in parentheses are percentages.
*$P < 0.05$, †$P < 0.01$, §$P < 0.0001$.
PML, Primary mediastinal lymphoma; GCT, germ cell tumor; SCLC, small cell lung cancer; NA, not applicable.

conducted independently of the CT analysis. All patients with PML underwent treatment, which included chemotherapy and radiotherapy for HL, chemotherapy and/or radiotherapy for Med-DLBCL, and chemotherapy and radiotherapy for T-LBL. Follow-up documentation was reviewed for any evidence of misdiagnosis at any repeat imaging examinations, biopsies, laboratory tests, or on the basis of ongoing symptoms and signs. At the time of this review, there has been no case of initial misdiagnosis.

To determine whether or not CT findings can accurately differentiate PML from the other common nonlymphomatous diseases, a total of 70 patients including thymoma (n = 19), thymic cancer (n = 26), germ cell tumor (n = 13), and small cell lung cancer (n = 12) were also enrolled in this study (Table 1). Selective criteria of these cases were 1) main anterior mediastinal mass identified on CT at presentation, 2) definite diagnosis confirmed by the pathologic observation of main mass, and 3) CT examination performed prior to therapy. These cases were selected from the radiologic files of our institute, and clinical details and follow-up information were also reviewed retrospectively by a radiologist who was one of the authors.

Imaging Studies

CT was performed on a 4-row multidetector scanner (Aquilion V-detector, Toshiba Medical Systems, Tokyo, Japan). The images were obtained at 240–260 mAs, 120 kV, 7-mm collimation sections overlapped in 3.5-mm intervals from the level of the orbit to the proximal femur, and a pitch of 10.5. All patients received 150 mL of nonionic intravenously administered contrast material at 3.0 mL/s with a power injector (Autoenhance A-250; Nemoto-kyorindo, Tokyo, Japan) after a 60-second delay. All patients also received 200–300 mL of sterile water orally prior to CT examination.

Image Analysis

Two experienced radiologists who had knowledge of the diagnosis of primary mediastinal lymphoma but were blinded to histologic subtypes and any clinical information other than patient age and sex independently reviewed the CT images on hard copies. The 2 readers analyzed the images for tumor size, tumor margins (well defined or ill defined), and presence of surface lobulation. The presence of a single mass or confluent lymphadenopathy in the anterior mediastinum was analyzed as representing the primary tumor mass and the measurement based on the short axis diameter. The contrast enhancement of the primary lesions was compared with that of normal muscle. The tumor was considered homogeneous if it enhanced to the same degree throughout. The patterns of local invasion were recorded: encasement of vascular structures, chest wall invasion, cutaneous involvement, and lung invasion. Vascular encasement was considered present when there was circumferential narrowing or complete obstruction of the superior vena cava or brachiocephalic vein by tumor. The presence or absence of lymphadenopathy, pleural effusion, pericardial effusion, and other organ involvement were also evaluated. Nodes were considered enlarged when their short axis diameter was greater than 10 mm. Hepatomegaly and splenomegaly were considered present when the liver and spleen were greater than 13 cm and 12 cm in longitudinal diameter at the midclavicular line, respectively.[29]

Statistical Analysis

Kruskal-Wallis test was used to compare the clinical variables and all CT findings in the 3 histologic subtypes of PML and the other common nonlymphomatous disorders. Student t test was used to compare mean tumor size of the mediastinal mass. The interobserver variation in the interpretation of all CT findings was analyzed using Kappa statistics. The interobserver agreement was classified as follows: poor, k = 0–0.20; fair, k = 0.21–0.40; moderate, k = 0.41–0.60; good, k = 0.61–0.80; and excellent, k = 0.81–1.00. The relationship between CT findings and the likelihood of the histologic subtypes was tested for independent predictors using multiple logistic regression analysis, which determined the odds ratio after adjusting for the other variables examined. All P values less than 0.05 were considered to indicate a statistically significant difference.

RESULTS

Statistically significant CT findings which have possibility of discriminating PML from the other common nonlymphomatous diseases were tumor margins, the presence of lung invasion, involvement of various lymph nodes including cervical (superficial and deep), mediastinal, hilar, axillary, paraaortic, inguinal lymph nodes, the presence of pericardial effusion, splenomegaly, the presence of lung metastasis, and liver metastasis. Patient demographics are listed in Table 2. Patients with Med-DLBCL were slightly older (mean age ± SD: 46.4 ± 18.0) than those with HL (34.6 ± 10.7) or T-LBL (30.6 ± 12.4) ($P < 0.01$). No other significant difference was seen in patient demographics between the 3 subtypes of PML.

TABLE 2. Demographic and Clinical Data in Patients With PML

Disease	HL	Med-DLBCL	T-LBL
No. of patients	29 (44)	21 (32)	16 (24)
Age (mean ± SD) (y)	34.6 ± 10.7	46.4 ± 18.0	30.6 ± 12.4*
Age range (y)	19–57	23–84	13–64
Gender			
Male	17 (59)	15 (71)	13 (81)
Female	12 (41)	6 (29)	3 (19)
IPI score			
Low	23 (79)	12 (57)	6 (38)
Low–intermediate	5 (17)	2 (10)	8 (50)
Intermediate–high	0	5 (24)	1 (6)
High	1 (3)	2 (10)	1 (6)
Clinical stage			
I	7 (24)	11 (52)	2 (13)
II	15 (52)	3 (14)	2 (13)
III	4 (14)	1 (5)	3 (19)
IV	3 (10)	6 (29)	9 (56)

Data in parentheses are percentages. Significant difference is found in the mean age between Med-DLBCL and T-LBL (*$P < 0.01$).

HL, Hodgkin lymphoma; Med-DLBCL, mediastinal diffuse large B-cell lymphoma; T-LBL, T-cell lymphoblastic lymphoma; IPI, International Prognostic Index.

Enlargement of cervical lymph nodes was seen more commonly in T-LBL (10 of 16 patients, 63%) than in HL (9 of 29 patients, 31%) ($P < 0.05$) and was not present in any of the patients with Med-DLBCL (Fig. 1). Of the cervical nodes, deep cervical nodes were affected more frequently in HL (31% [9 of 29 patients]) or T-LBL (56% [9 of 16 patients]) than those in Med-DLBCL (no patients). Superficial nodes were also involved more often in T-LBL (44% [7 of 16 patients]) than in HL (10% [3 of 29 patients], $P < 0.05$). Involvement of supraclavicular lymph nodes was seen more frequently in T-LBL (50% [8 of 16 patients]) compared with that in HL (10% [3 of 29 patients], $P < 0.01$). Submandibular, submental, and parotid lymph nodes were involved only in T-LBL (19% [3 of 16 patients]).

No significant difference was found in the size and margin of the primary lesion between the three histologic subtypes (Table 3). Surface lobulation (Fig. 2) was more common in HL (69% [20 of 29 patients]) than in both Med-DLBCL (33% [7 of 21 patients]) and T-LBL (25% [4 of 16 patients]) ($P < 0.01$, Table 3). The prevalence of vascular involvement including encasement of superior vena cava and left brachiocephalic vein in Med-DLBCL (62% [13 of 21 patients], $P < 0.0001$) and T-LBL (38% [6 of 16 patients],

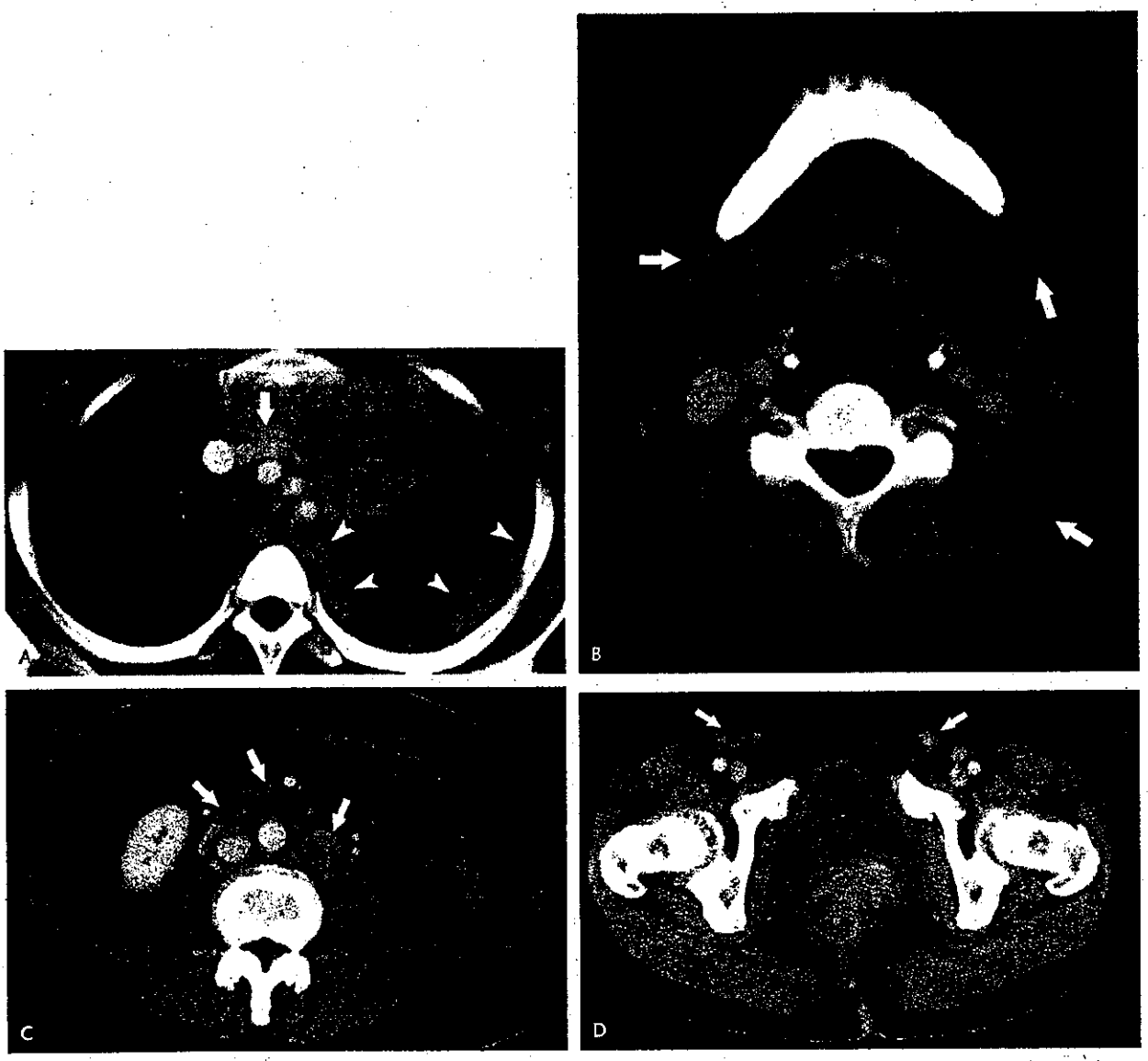

FIGURE 1. Thirty-two-year-old man with T-cell lymphoblastic lymphoma (T-LBL). A, Image obtained at the level of the great vessels shows a large anterior mediastinal mass with encasement and stenosis of the left brachiocephalic vein (arrow). Also noted are left pleural effusion and soft-tissue masses (arrowheads) in the left pleura suggestive of pleural dissemination. B, Image at the level of the upper neck demonstrates several enlarged of cervical nodes (arrows). C, Image at the level of the lower pole of the right kidney shows multiple enlarged paraaortic and mesenteric nodes. D, Image at the level of the inguinal region shows enlarged inguinal lymph nodes (arrows).

TABLE 3. CT Findings in Patients With PML

Disease	HL	Med-DLBCL	T-LBL
No. of patients	29 (44)	21 (32)	16 (24)
Tumor margins			
Well-defined margins	19 (66)	10 (48)	10 (62)
Ill-defined margins	10 (34)	11 (52)	6 (38)
Size of main mass (mean ± SD) (cm)	9.7 ± 2.8	9.7 ± 2.5	10.2 ± 3.3
Presence of surface lobulation*	20 (69)	7 (33)	4 (25)
Presence of vasular encasement†	2 (7)	13 (62)	6 (38)
Presence of chest wall invasion	4 (14)	4 (19)	2 (13)
Presence of cutaneous involvement	0	2 (10)	1 (6)
Presence of lung invasion	8 (28)	2 (10)	1 (6)
Presence of nodal involvement			
Cervical lymph node (superficial)*	3 (10)	0	7 (44)
Cervical lymph node (deep)†	9 (31)	0	9 (56)
Submandibular lymph node	0	0	1 (6)
Submental lymph node‡	0	0	2 (13)
Parotid lymph node‡	0	0	2 (13)
Supraclavicular lymph node§	3 (10)	0	8 (50)
Mediastinal lymph node†	28 (97)	14 (67)	8 (50)
Hilar lymph node‡	10 (34)	1 (5)	1 (6)
Axillary lymph node†	4 (14)	0	8 (50)
Celiac lymph node	3 (10)	0	1 (6)
Paraaortic lymph node*	6 (21)	0	6 (38)
Mesenteric lymph node‡	0	0	2 (13)
Iliac lymph node	0	0	1 (6)
Inguinal lymph node†	0	0	5 (31)
Presence of pleural effusion‡	6 (21)	12 (57)	8 (50)
Presence of pericardial effusion‡	5 (17)	10 (48)	9 (56)
Hepatomegaly‡	0	0	2 (13)
Splenomegaly†	1 (3)	1 (5)	11 (63)

Date in parentheses are percentages.
*$P < 0.01$, †$P < 0.001$, ‡$P < 0.05$, §$P < 0.0001$.
HL, Hodgkin lymphoma; Med-DLBCL, mediastinal diffuse large B-cell lymphoma; T-LBL, T-cell lymphoblastic lymphoma.

$P < 0.05$) was greater than that in HL (7% [2 of 29 patients], Figs. 1 and 2). Complete obstruction of the superior vena cava (SVC syndrome) was present in one of 29 patients with HL (3%), 4 of 21 with Med-DLBCL (19%), and 2 of 16 patients with T-LBL (13%). Forty-one of 66 tumors (62%) showed heterogeneous enhancement on CT, with no significant difference between 3 histologic subtypes.

Enlarged mediastinal nodes distinct from the primary lesion were present more commonly in HL (97% [28 of 29 patients]) than in Med-DLBCL (67% [14 of 21 patients], $P < 0.05$) and T-LBL (50% [8 of 16 patients], $P < 0.0001$, Table 3). Involvement of hilar nodes (Fig. 3) was significantly more common in HL (34% [10 of 29 patients]) compared with Med-DLBCL (5% [1 of 21 patients], $P < 0.05$) and T-LBL (6% [1 of 16 patients], $P < 0.05$). Involvement of bilateral axillary nodes was significantly more common in T-LBL (50% [8 of 16 patients]) than in Med-DLBCL (no patients, $P < 0.0001$) and HL (14% [4 of 29 patients], $P < 0.05$). Pleural effusion (Figs. 1 and 2) was significantly more common in Med-DLBCL (57% [12 of 21 patients], $P < 0.01$) or T-LBL (50% [8 of 16 patients], $P < 0.05$) than in HL (21% [6 of 29 patients]). Of the patients with pleural effusion, tumor cells were confirmed by cytology in 6 of 6 patients with HL (100%), in 5 of 12 with Med-DLBCL (42%), and in 2 of 8 patients (25%) with T-LBL. Pericardial effusion (Fig. 4) was significantly more common in T-LBL (56% [9 of 16 patients], $P < 0.01$) and Med-DLBCL (48% [10 of 21 patients], $P < 0.05$) than in HL (17% [5 of 29 patients]).

Statistically significant CT findings in the abdomen included splenomegaly, and involvement of paraaortic, mesenteric, and inguinal lymph nodes (Table 3). Splenomegaly was present more commonly in T-LBL (63% [11 of 16 patients]) than in HL (3% [1 of 29 patients], $P < 0.0001$) and Med-DLBCL (5% [1 of 21 patients], $P < 0.0001$). Involvement of abdominal paraaortic nodes (Fig. 1) was more common in T-LBL (38% [6 of 16 patients], $P < 0.01$) or HL (21% [6 of 29 patients], $P < 0.05$) than in Med-DLBCL (no patients). Involvement of inguinal (31% [5 of 16 patients]) or mesenteric lymph nodes (13% [2 of 16 patients]) was found only in T-LBL (Fig. 1). Extranodal lesions in the abdomen were proved pathologically in 3 patients. Two patients with Med-DLBCL had mass lesions in the stomach and kidney, and the